Journal of Applied Physics

Lateral transport in silicon solar cells

Cite as: J. Appl. Phys. **127**, 114501 (2020); https://doi.org/10.1063/1.5139416
Submitted: 19 November 2019 . Accepted: 25 February 2020 . Published Online: 16 March 2020

Jan Haschke, Gabriel Christmann, Christoph Messmer, Martin Bivour, Mathieu Boccard, and Christophe Ballif

ARTICLES YOU MAY BE INTERESTED IN

Influence of local surface defects on the minority-carrier lifetime of passivating-contact solar cells
Applied Physics Letters **116**, 113901 (2020); https://doi.org/10.1063/1.5145351

Passivating contacts and tandem concepts: Approaches for the highest silicon-based solar cell efficiencies
Applied Physics Reviews **7**, 021305 (2020); https://doi.org/10.1063/1.5139202

Impact of carrier recombination on fill factor for large area heterojunction crystalline silicon solar cell with 25.1% efficiency
Applied Physics Letters **107**, 233506 (2015); https://doi.org/10.1063/1.4937224

Your Qubits. Measured.
Meet the next generation of quantum analyzers

- Readout for up to 64 qubits
- Operation at up to 8.5 GHz, mixer-calibration-free
- Signal optimization with minimal latency

Find out more

© 2020 Author(s).

Journal of Applied Physics ARTICLE scitation.org/journal/jap

Lateral transport in silicon solar cells

Cite as: J. Appl. Phys. **127**, 114501 (2020); doi: 10.1063/1.5139416
Submitted: 19 November 2019 · Accepted: 25 February 2020 ·
Published Online: 16 March 2020

View Online

Export Citation

CrossMark

Jan Haschke,[1,a)] Gabriel Christmann,[2] Christoph Messmer,[3] Martin Bivour,[3] Mathieu Boccard,[1,b)] and Christophe Ballif[1,2]

AFFILIATIONS

[1]Ecole Polytechnique Fédérale de Lausanne (EPFL), Institute of Microengineering, Photovoltaics and Thin-Film Electronics Laboratory (PV-LAB), Rue de la Maladière 71B, CH-2002 Neuchâtel, Switzerland
[2]Swiss Center for Electronics and Microtechnology (CSEM), PV-center, Rue Jaquet Droz 1, CH-2002 Neuchâtel, Switzerland
[3]Fraunhofer Institute for Solar Energy Systems (ISE), Heidenhofstrasse 2, D-79110 Freiburg, Germany

[a)]jan.haschke.pv@gmail.com. **Present address:** REC Solar Pte. Ltd., 20 Tuas South Ave. 14, Singapore 637312, Singapore.
[b)]**Author to whom correspondence should be addressed:** mathieu.boccard@epfl.ch

ABSTRACT

We investigate lateral charge carrier transport in crystalline silicon solar cells. Under typical operation illumination of high-efficiency solar cells, a significant population of electrons and holes exist in the silicon wafer, leading to a non-negligible sheet conductance for both carrier types. To investigate the contribution of these sheet conductances to lateral transport in solar cells, we develop a model that calculates the effective series resistance of two sheet resistances coupled via a contact resistance. In solar cells, the upper sheet resistance describes the highly conductive region like a diffusion or a transparent conductive oxide, whereas the lower sheet resistance describes the silicon absorber. We find that the coupling contact resistance needs to be low to benefit from the lateral current flow in the silicon absorber. We show experimentally for silicon heterojunction solar cells that the silicon absorber supports lateral minority charge carrier transport for well-passivated devices. Another finding is that there is no principle advantage for coupling of the two sheet resistances for rear-junction or front-junction solar cells, as the *pn*-junction (for front-junction solar cells) does not prevent coupling. We suggest that for n-type silicon heterojunction solar cells, the observed advantage of the rear-junction over the front-junction architecture is due to practically lower contact resistance and higher mobility of electrons vs holes. We also confirm experimentally the importance of a low contact resistivity between the highly conductive region and the silicon absorber for effective coupling and present an innovative technique to extract contact resistance from comparing Suns-V_{OC} and current–voltage measurements.

Published under license by AIP Publishing. https://doi.org/10.1063/1.5139416

I. INTRODUCTION

In wafer-based silicon solar cells, charge carriers have to travel laterally toward grid-fingers, which usually happens in highly conductive regions: n^+ or p^+ diffusions.[1] In emerging devices with so-called passivating contacts, often a transparent conductive oxide (TCO) is used to provide lateral conductivity[2–6] as the diffusion is too shallow or the doped layers are too thin to provide sufficient lateral conductivity, and the latter is the case for, e.g., silicon heterojunction (SHJ) solar cells.[5] Given its conductivity is high enough, the silicon absorber can also contribute to lateral transport. For example, industrial increasingly common so-called PERC (passivated emitter and rear cell) devices rely on lateral majority carrier transport in the absorber.[7]

Under illumination, excess charge carriers are provided, which increase the conductivity of the absorber. This is referred to as conductivity modulation in the literature.[8–10] While the modulation of the conductivity for majority charge carriers is relatively small, especially for highly doped absorbers, the effect is much more pronounced for minority charge carriers. Under 1-sun illumination, their concentration usually increases by over ten orders of magnitude and, as a consequence, the minority-charge-carrier conductivity of the absorber is drastically increased. Whether it is high enough to support lateral minority-charge-carrier transport depends on the level of passivation and the intensity of the illumination.[9] Similar carrier density for electrons and holes is obtained in a well-passivated silicon absorber under 1-sun illumination, and the difference in hole sheet conductance vs electron sheet conductance is mainly due to the difference in mobility.

Despite the similar carrier concentrations of electrons and holes under illumination, lateral transport of minority carriers in a

Published under license by AIP Publishing.

silicon absorber is rarely considered for the loss analysis of a solar cell's series resistance. This might be due to the fact that, in the past, the sheet resistance for the minority carriers in a silicon absorber was usually high due to insufficient passivation of the solar cells and the resulting low minority-carrier density. This will be further discussed below. Instead, lateral minority-carrier transport was indeed predominantly happening in, e.g., the front-surface diffusion of a front-junction solar cell.

With the emergence of silicon solar cells with passivated contacts, however, the minority-carrier density at maximum power point (MPP) becomes sufficiently high to provide lateral conductivity.

Silicon heterojunction (SHJ) solar cells feature excellent passivation, and thus high minority charge carrier densities at MPP, as well as diffusion lengths of several millimeters. Still, lateral transport of minority carriers in the silicon absorber is usually not considered when breaking down series resistance losses. This might be due to the misconception that the *pn*-junction would block the coupling of TCO and silicon absorber. Indeed, it is stated that the silicon absorber can support lateral (majority carrier) transport when the minority charge carrier collecting junction is at the rear.[5,11–15]

In agreement with Refs. 16 and 17 (In Ref. 16, classical silicon solar cells with diffused contacts are discussed. However, the functional principle applies also to solar cells where two-layer lateral transport is not provided by diffused regions but, e.g., TCOs.), we would like to underline that lateral minority charge carrier transport can generally also happen in the silicon absorber. In an earlier publication,[18] we showed experimentally that neglecting lateral transport in the silicon absorber of SHJ front-junction devices can lead to faulty breakdown of the R_S losses. When the sheet resistance for holes in the silicon absorber, $R^{h^+}_{\square,\mathrm{Si}}$, is not taken into account for lateral transport, the remaining resistance attributed, e.g., to the p-contact is overestimated. In our earlier publication,[18] however, we neglected the coupling contact resistance ρ_c between silicon absorber and TCO and assumed the two layers as parallel resistances [cf. Eq. (1)].

While classical solar cell devices with diffused contacts do not feature a contact resistance between the two conductive layers, solar cells with passivating contacts usually do. Here, we develop a model that considers a contact resistance for the coupling of two conductive layers. We use the same approach as Huang *et al.*[19] but modify the model to be applicable to solar cells. We validate our model with numerical simulations and show experimentally that for front-junction SHJ devices lateral transport in the silicon absorber is relevant, depending on the injection level in the device and ρ_c. Furthermore, we discuss that the advantage of rear-junction (Often referred to as "rear emitter" devices. As "emitter" is a misnomer regarding photovoltaics,[1] we use rear-junction as identifier.) devices is not the fact that the *pn*-junction is at the rear but the higher likelihood that prerequisites for lateral transport in the silicon absorber is fulfilled (cf. Sec. II A).

For SHJ devices, with total series resistances of $0.2\,\Omega\,\mathrm{cm}^2$ for the whole device,[20] the accurate untangling of the different series resistance components for device analysis and optimization becomes increasingly challenging. Our model enables the consideration of lateral transport in the silicon absorber without the need for time consuming numerical simulations and offers a method to evaluate contact resistance in the device from standard current–voltage, Suns-V_{OC}, and sheet resistance measurements.

For all the calculations or numerical simulations in this paper, the silicon absorber is n-type, with a resistivity of $2\,\Omega\,\mathrm{cm}$ ($N_D = 2.382\times10^{15}\,\mathrm{cm}^{-3}$) and a thickness of $180\,\mu$m. If not stated otherwise, the pitch (grid-finger distance), p, is $1850\,\mu$m, the finger-width, w_f, is $50\,\mu$m, and the contact resistance between TCO and Ag, $\rho_c^{\mathrm{TCO/Ag}}$, is $1\,\mathrm{m}\Omega\,\mathrm{cm}^2$. This corresponds also to the parameters of the experimental devices discussed in this paper.

II. COUPLING TWO SHEET RESISTANCES VIA A CONTACT RESISTANCE IN SILICON SOLAR CELLS

As described above, lateral transport in silicon solar cells happens usually either in a highly conductive region or the silicon absorber. In the case of SHJ solar cells, the highly conductive region is the TCO of the respective contact. Although the principle applies also to silicon solar cells with diffused regions, in the following, we limit the discussion and the identifiers to SHJ solar cells for simplicity.

For the calculation of the effective sheet resistance for SHJ rear-junction solar cells Refs. 11, 13, 14, 17, 18, 21, and 22 assume the sheet resistance of the TCO, $R_{\square,\mathrm{TCO}}$, and silicon absorber, $R_{\square,\mathrm{Si}}$,

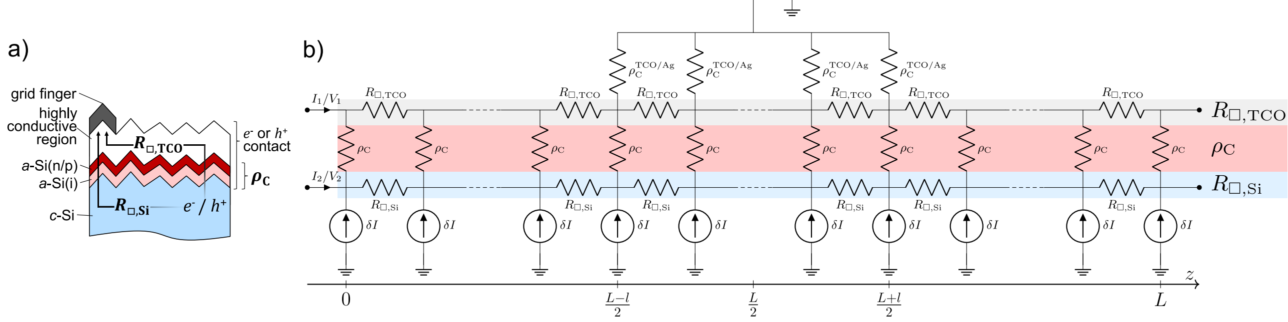

FIG. 1. (a) Scheme of possible lateral current flows in solar cells (half pitch). For silicon heterojunction solar cells, the highly conductive region is usually realized with a transparent conductive oxide (TCO). (b) Equivalent circuit of the analytical model developed in this work (full pitch).

Published under license by AIP Publishing.

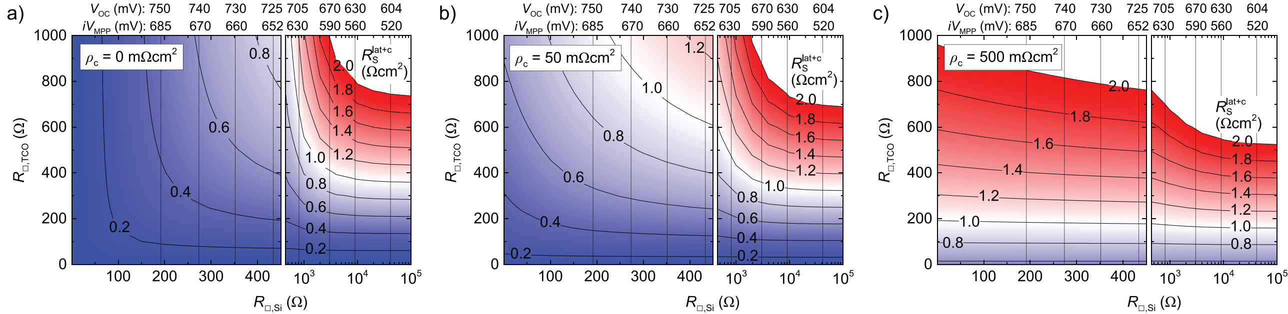

FIG. 2. Contour plots of the resulting resistance (R_S^{lat+c}) of two stacked sheet resistances coupled via a contact resistance ρ_c for a ρ_c of (a) 0 mΩ cm^2, (b) 50 mΩ cm^2, and (c) 500 mΩ cm^2. Contour lines with labels indicate iso-R_S^{lat+c} conditions. Vertical lines indicate specific $R_{\square,Si}^{h^+}$ corresponding to different injection levels at MPP in a 180 μm 2 Ω cm n-type silicon absorber. For reference, the implied voltage at MPP and typical corresponding V_{OC} values are indicated on the top axis. The $R_{\square,Si}^{e^-}$ value of the absorber in the dark is 111 Ω.

as two parallel resistances,

$$R_{\square,\parallel} = \left(R_{\square,\,Si}{}^{-1} + R_{\square,\,TCO}{}^{-1}\right)^{-1}. \quad (1)$$

However, Eq. (1) is a simplification. As depicted in Fig. 1(b), the two sheet resistances are coupled via the contact resistance ρ_c in the device. Thus, Eq. (1) is an approximation and mathematically valid only [The approximation comes close to the model including ρ_c, for very low $R_{\square,TCO}$, or when ρ_c is "low enough" (cf. Fig. 5). The concrete definition of "low enough" depends, however, on the interplay of $R_{\square,TCO}$, $R_{\square,Si}$, ρ_c, and the finger-pitch p.] when $\rho_c = 0\,\Omega\,cm^2$, which will be further discussed in Sec. II A.

We set up a model that solves the current flow in two parallel conducting layers coupled via a contact resistance and use it to calculate the resulting effective resistance. As this resistance is due to lateral- as well as contact resistance, we call it R_S^{lat+c} in the following. The equivalent circuit (full pitch) is depicted in Fig. 1(b), and a more detailed description of the model is given in Appendix A. The model yields the same results as a (sufficiently high-resolution) SPICE model.

A. Impact of the contact resistance and prerequisites for lateral current flow in the silicon absorber

Using our model, we varied the silicon absorber and TCO sheet resistances for three different values of contact resistances and show contour plots of the resulting resistance R_S^{lat+c} in Figs. 2(a)–2(c). When ρ_c is zero, lateral transport can happen equally in the TCO or the silicon absorber, as can be seen in Fig. 2(a). For the case of $\rho_c = 500\,m\Omega\,cm^2$ [cf. Fig. 2(c)], the resulting R_S^{lat+c} is much less dependent on the silicon absorber's sheet resistance, suggesting that lateral transport mostly happens in the TCO. Resistive losses due to lateral transport are dominated by the sheet resistance of the TCO. Still, for a (relatively high) $R_{\square,TCO}$ of 300 Ω, the R_S^{lat+c} is reduced by about 0.2 Ω cm^2, when the sheet resistance of the silicon absorber is low. Such a low $R_{\square,Si}$ can be provided by excess holes (front-junction device on n-type silicon), or when electrons as majority carriers provide sufficient conductivity. In Figs. 2(a)–2(c), we indicate with vertical lines hole sheet resistances $R_{\square,Si}^{h^+}$, corresponding to different injection levels in an n-type silicon absorber. The value of $R_{\square,Si}^{h^+}$ is to be read on the lower x axis, as $R_{\square,Si}$. On the upper x axis, we give the injection level as implied voltage at MPP (iV_{MPP}) and a typical value for the corresponding V_{OC} derived from numerical simulations (see below). The $R_{\square,Si}^{e^-}$ value of the absorber in the dark is 111 Ω.

In Figs. 2(a)–2(c), we showed under which conditions lateral transport in the silicon absorber can lower the series resistance of the device. We found that there are three **prerequisites for significant lateral current flow in the silicon absorber**,

1. sufficient sheet conductance for the considered carriers in the silicon absorber,
2. low-enough contact resistance between the contact's TCO and the silicon absorber, and
3. relatively high $R_{\square,TCO}$ vs $R_{\square,Si}$, as when $\rho_c > 0\,\Omega\,cm^2$, lateral transport is preferably happening in the TCO; only for $\rho_c = 0\,\Omega\,cm^2$, the current distribution is equal between TCO and silicon when their respective $R_\square$ are equal.

This underlines the importance of a low contact resistance to obtain highest efficiencies. A low contact resistance reduces not only the vertical transport losses (carriers crossing the contacts) but also lateral transport losses, as it enables the support for lateral transport in the absorber.

The model is describing the general case of two conducting layers connected via a contact resistance. For SHJ solar cells, the ρ_c of the model corresponds to the effective contact resistance of an a-Si(i/p)/TCO or an a-Si(i/n)/TCO stack. The model is thus assuming that holes/electrons in the silicon absorber and electrons from the TCO are coupled as described in Fig. 1(b). It is, therefore, not taking into account a pn-junction, which may be present between the two conducting layers in, e.g., front-junction or bifacial rear-junction devices.

Published under license by AIP Publishing.

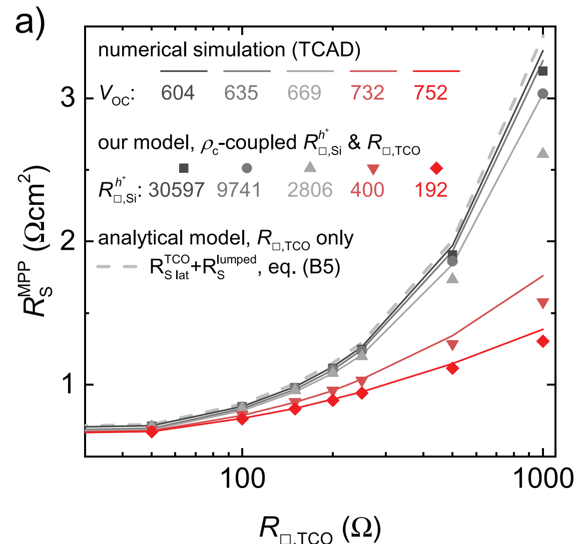

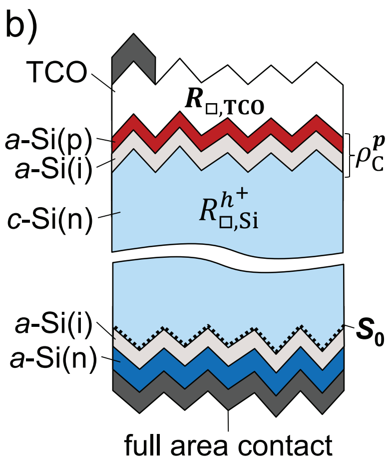

FIG. 3. (a) Comparison of R_S^{lat+c} from our model to calculate the effective R_S of two sheet resistances (silicon absorber and front-side TCO) coupled via ρ_c (symbols). Solid lines: series resistance at MPP of front-junction SHJ devices with varying $R_{\square,TCO}$ (x axis) and five different injection levels, numerically simulated with Sentaurus TCAD. Dashed gray line: analytical calculation of R_S^{MPP} assuming lateral transport only in the front TCO [Eq. (B5)] and an additional lumped R_S. (b) Scheme of the simulated structure.

B. Validation of the model for lateral transport of minority carriers

To validate the approach for the cases in which the role of the *pn*-junction is not clear from the literature (cf., e.g., Refs. 11–15), we performed numerical simulations using Sentaurus TCAD. We set up a front-junction (FJ) SHJ device with a unit cell as depicted in Fig. 3(b), and varied $R_{\square,TCO}$ and the surface recombination velocity at the rear side. With the latter, we obtain five different injection conditions leading to simulated devices with V_{OC} values from 604 mV to 752 mV, where the latter is the Auger limit for the used absorber. The front-side *a*-Si(i/p)/TCO stack is modeled as described in Appendix C and yields a low ρ_c^p, no additional specific contact resistances were assumed for any of the interfaces between TCO and silicon absorber. This should enable efficient coupling between the minority-carrier sheet resistance $R^{h^+}_{\square,Si}$ and $R_{\square,TCO}$. From the simulation, we calculate $R_S^{MPP}$and pV_{MPP} following the approach of Bowden and Rohtagi as described in Appendix D, for the five injection conditions.

We calculate R_S^{MPP} also with our model for R_S^{lat+c} at the front side, and additional R_S components to match the simulations, as detailed in Appendix D. For our model, we assume a ρ_c^p of $0.04\,\Omega\,cm^2$, as it fits best the simulation.

In Fig. 3, we show R_S^{MPP} obtained with the two methods. For further comparison, as gray dashed line, we show also an R_S^{MPP} resulting from lateral transport in TCO only. This was calculated with Eq. (B5) for the different $R_{\square,TCO}$ and adding the same additional R_S-components as for our model.

For $R_{\square,TCO}$ between $0\,\Omega$ and $500\,\Omega$, our model fits well the numerical simulation, with a deviation of our model from the simulated values below 3%. For $R_{\square,TCO} = 1000\,\Omega$, model and simulation deviate more, up to 14% for the devices with a V_{OC} of 669 mV. This might be due to the analysis of Bowden and Rohtagi becoming less accurate for relatively high R_S. As a result, also the extracted pV_{MPP} values are subject to a relatively large uncertainty. As for the devices with a V_{OC} of 669 mV, rather small differences in voltage will lead to relatively large differences in $R^{h^+}_{\square,Si}$ at MPP, this could explain why the deviation is the highest for this case.

Despite these uncertainties, the R_S values obtained from our model follow well the R_S values calculated from the numerical simulations. Solar cells with $V_{OC} \leq 635$ mV can be described assuming only lateral transport in the TCO. For solar cells with V_{OC} above 700 mV, transport in the silicon wafer needs to be taken into account for accurate results, especially when $R_{\square,TCO}$ is high. Such V_{OC} values are obtained by silicon heterojunction solar cells and also by many other premium solar cells currently manufactured with classic high-temperature diffusion. With the emergence of SHJ and high-temperature passivating contacts,[23–26] this will be relevant for many (industrial) solar cells in the coming years.

The numerical simulations show that it is a misconception that the *pn*-junction is blocking the coupling of the conductances of silicon absorber and TCO. Thus, our simple model is generally valid for the analysis of lateral transport paths in silicon solar cells. There is no principle difference between rear-junction and front-junction devices for lateral transport.

C. Specifics of front- vs rear-junction SHJ devices

In the SHJ literature, for both experiment[11,21] and simulation,[11,15,27] it was found that rear-junction (RJ) devices benefit from lateral transport in the silicon absorber, while front-junction devices do not. Usually, the contact at the front-side of SHJ front-junction devices is the p-contact. For this contact, contact resistance values in the range of $300-500\,m\Omega\,cm^2$ are given in the literature.[13,17,28–31] For the n-contact, lower values down to $50\,m\Omega\,cm^2$ are given. The latter can be considered as a good n-contact.[28,29,32,33] As can be seen from Fig. 2(b) for such low ρ_c the support of the silicon absorber in lateral transport is much more pronounced. With the insights from Sec. II, we thus conclude that the advantage of the rear-junction configuration of SHJ solar cells in practice is due to

Published under license by AIP Publishing.

- most rear-junction SHJ cells being based on n-type silicon, i.e., the relevant contact is the n-contact,
- ρ_c of the n-contact being lower than of the p-contact,[13,17,28–30] thus enabling better coupling,
- the reported rear-junction SHJ cells being monofacial cells, which means that lateral transport in the bulk is (potentially) only relevant for the charge carriers collected at the front contact, and
- the mobility of electrons vs holes being about three times higher, thus at equal carrier concentrations, $R_{\square,\mathrm{Si}}$, is three times lower for electrons vs holes.

To illustrate the points above, we calculated the injection-dependent $R_S^{\mathrm{lat+c}}$ for front-junction (FJ) and rear-junction (RJ) cases for an n-type silicon absorber and contact geometry as stated at the end of the Introduction. We assume monofacial cells, thus lateral transport is only relevant for the charge carriers traveling to the front contact, as the full-area rear metallization provides abundant lateral sheet conductance [cf. Figs. 4(c) and 4(d)]. We compare 100 Ω and 500 Ω for the TCO sheet resistance, as we found 500 Ω to be the upper limit of what is reported in the literature for $R_{\square,\mathrm{TCO}}$ for RJ devices,[11,15,21] and 100 Ω being a value typically used for front-junction SHJ devices.[34] In the calculation, the FJ and RJ cases only differ in the injection-dependent $R_{\square,\mathrm{Si}}$, due to the difference in hole/electron concentration and mobility. We assume a range between 645 mV and 685 mV for the implied voltage at MPP.

As shown in Fig. 4(a), for a contact resistance of 0.4 Ω cm^2 and $R_{\square,\mathrm{TCO}}$ of 100 Ω, there is only a minor difference in $R_S^{\mathrm{lat+c}}$ between the FJ and RJ case (≈0.01 Ω cm^2 at 0.645 V). This is the case despite $R_{\square,\mathrm{Si}}$ being a factor of four to seven lower for the RJ case, as indicated on the upper x axis. This means that lateral conductivity is mainly provided by the TCO for both front and rear-junction case. For a $R_{\square,\mathrm{TCO}}$ of 500 Ω, as shown in Fig. 4(b), the difference between RJ and FJ case is larger but still only amounts to 0.14 Ω cm^2 at an implied voltage of 645 mV. When reducing ρ_c, however, the calculated $R_S^{\mathrm{lat+c}}$ differ significantly between front and rear-junction case, especially for $R_{\square,\mathrm{TCO}} = 500\,\Omega$. For $\rho_c = 0.05\,\Omega\,\mathrm{cm}^2$, the difference at 645 mV amounts to 0.36 Ω cm^2, indicating lower lateral resistance for the RJ case, due to transport in the silicon absorber.

To underline the importance of considering ρ_c for the R_S analysis of rear-junction cells, we calculated the effective R_S for silicon absorber, TCO, and contact resistance once with our model (This corresponds to what we refer to as $R_S^{\mathrm{lat+c}}$above.) (ρ_c-dependent coupling), and once assuming Eq. (1) to calculate $R_{\square,\parallel}$, as typically done in the literature, which corresponds to $\rho_c = 0\,\Omega\,\mathrm{cm}^2$. We assume an iV_{MPP} of 650 mV for a silicon absorber and front-grid geometry as above. For the model with $\rho_c = 0\,\Omega\,\mathrm{cm}^2$, the lateral R_S is then calculated using Eq. (B5) and $R_{\square,\parallel}$. Additionally, we add ρ_c and $\rho_c^{\mathrm{TCO/Ag}} \cdot p/w_f$ to be comparable with the results for ρ_c-dependent coupling. As shown in Fig. 5, the approach with $\rho_c = 0\,\Omega\,\mathrm{cm}^2$ is underestimating R_S as it overestimates the coupling between the TCO and the silicon absorber, especially for high contact resistances and high $R_{\square,\mathrm{TCO}}$. For a ρ_c of 0.001 Ω cm^2, both models yield similar results, but already for $\rho_c = 0.05\,\Omega\,\mathrm{cm}^2$ the models differ significantly for $R_{\square,\mathrm{TCO}} > 50\,\Omega$.

This underlines that also for RJ cells, $R_{\square,\mathrm{Si}}$ can only significantly contribute to lateral transport when ρ_c is low. For an accurate R_S analysis, ρ_c needs to be considered.

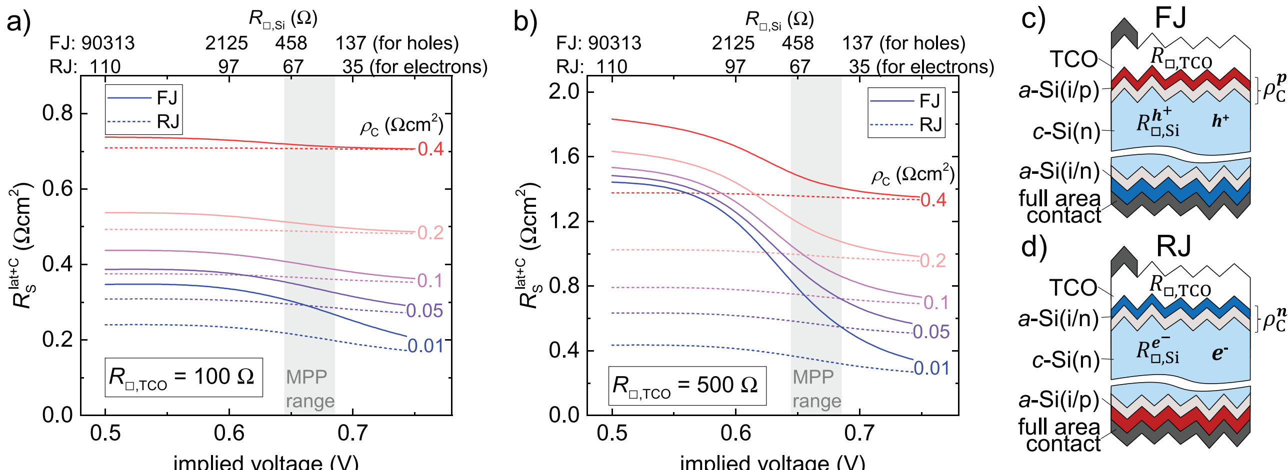

FIG. 4. Comparison of the resulting resistance $R_S^{\mathrm{lat+c}}$ vs implied voltage/injection for the front-junction (FJ) and rear-junction (RJ) cases for a series of contact resistances ρ_c. For a TCO sheet resistance of (a) 100 Ω and (b) 500 Ω. Indicated on the upper x axis are the sheet resistances of a 180 μm, 2 Ω cm, n-type silicon absorber for both the FJ (hole sheet resistance) and RJ (electron sheet resistance) cases. The gray area indicates the range of implied voltage at MPP corresponding to injection conditions for typical high-efficiency silicon solar cells. Please note the different scales of the y axis for (a) and (b). (c) and (d) show schemes of the considered front- and rear-junction cases, respectively.

Published under license by AIP Publishing.

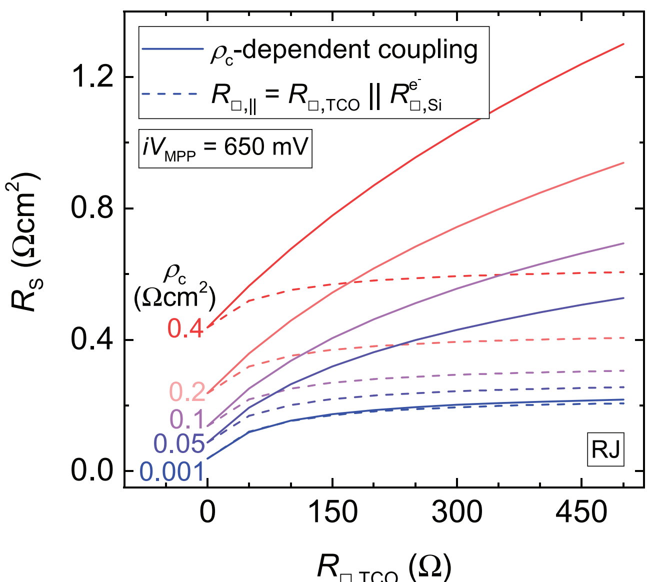

FIG. 5. Comparison of the R_S calculated for a rear-junction (RJ) device on an n-type silicon absorber with two methods: Dashed lines correspond to neglecting ρ_c-dependent coupling using Eqs. (1) and (B5). Solid lines correspond to the R_S calculated with our model accounting for ρ_c-dependent coupling, for ρ_c between 0.001 Ω cm^2 and 0.4 Ω cm^2. An iV_{MPP} of 650 mV was assumed which corresponds to a $R^{e^-}_{\square,Si}$ value of 67 Ω.

As shown by our calculations presented in Sec. II, the silicon absorber can support lateral conductivity of a specific charge carrier type (electrons or holes), when their concentration is high enough, and the contact resistance between silicon and TCO of the corresponding contact is low. To investigate if these conditions are met for our silicon heterojunction solar cells, and to experimentally access the impact of the injection level, we fabricated SHJ solar cells as described below.

1. Device fabrication and characterization

We prepared two groups of SHJ solar cells, which we refer to as low-injection (LI) and high-injection (HI) devices in the following. The two injection conditions result in two different $R^{h^+}_{\square,Si}$ at MPP in the silicon absorber. The HI devices feature *a*-Si(i) layers at both sides of the absorber, while for the LI devices, we omitted the *a*-Si(i) layer at the rear side as depicted in Fig. 6(b). This leads to lower effective lifetime and thus lower injection. In terms of V_{OC}, the LI devices are comparable with PERC solar cells. Different sheet resistances $R_{\square,TCO}$ of the front TCO were obtained by varying the O_2/Ar gas flow ratios between 0.01 and 0.06 during the deposition of Indium Tin Oxide (ITO), leading to sheet resistances in the range of 50−250 Ω. To keep the contact between ITO and *a*-Si(p) constant for all sheet resistances, we used an approximately 4 nm thin ITO contact layer that was deposited under identical conditions for all devices, using an O_2/Ar ratio of 0.02. Further details on device fabrication can be found in Ref. 35. We used 4 in. float-zone n-type wafers with a resistivity of 2 Ω cm and a thickness of 180 μm. Per $R_{\square,TCO}$ and group, we prepared one wafer that contains five 2×2 cm^2 solar cells.

Current-voltage (JV) measurements were performed at standard test conditions (STCs) with a dual-lamp Wacom AM1.5g solar simulator with class AAA characteristics. Besides STC, all solar cells were also measured at approximately 5.5 mW cm^{-2} intensity using a neutral density filter. From the two JV-curves, the series resistance at MPP, R_S^{MPP}, was calculated using the method from the literature.[36,37] With R_S^{MPP}, we then calculate the pseudo-voltage at MPP, pV_{MPP}, using Eq. (B3). The median, negative, and positive error values were calculated considering all five cells. $R_{\square,TCO}$ was measured four times with the four-point-probe technique on a grid-free area on the same wafer, as well as via TLM also on the same wafer. From these values, the average and standard deviation were calculated. The latter is generally lower than the symbol size in Fig. 7 and thus, error-bars in the x-direction are not included for clarity.

2. JV parameter and FF loss analysis

In Fig. 6(a), we show the JV-curves of the solar cells. As can be seen, the two groups feature significantly different V_{OC}, indicating the two different injection conditions for the two groups. With increasing $R_{\square,TCO}$ J_{SC} increases due to decreasing parasitic free

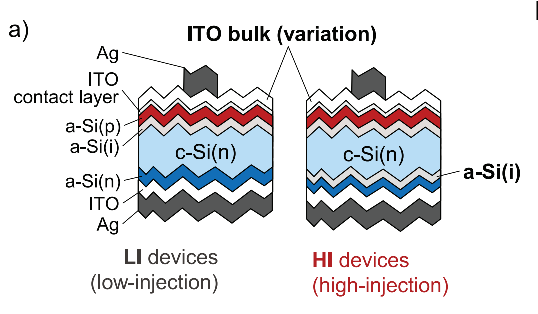

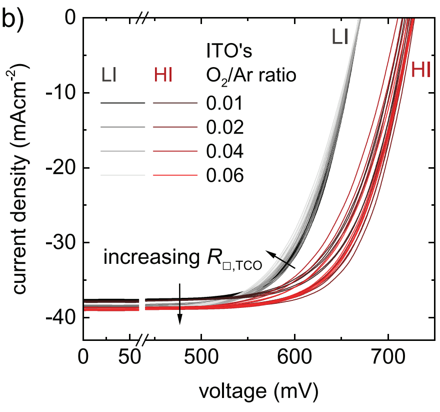

FIG. 6. (a) Cell schemes of the low-injection (LI) and high-injection (HI) devices. (b) JV-curves of LI (gray shades) and HI (red shades) devices. Lighter shades correspond to higher $R_{\square,TCO}$ (i.e., lower parasitic absorption), as a result of a higher O_2/Ar ratio during the deposition of the ITO.

Published under license by AIP Publishing.

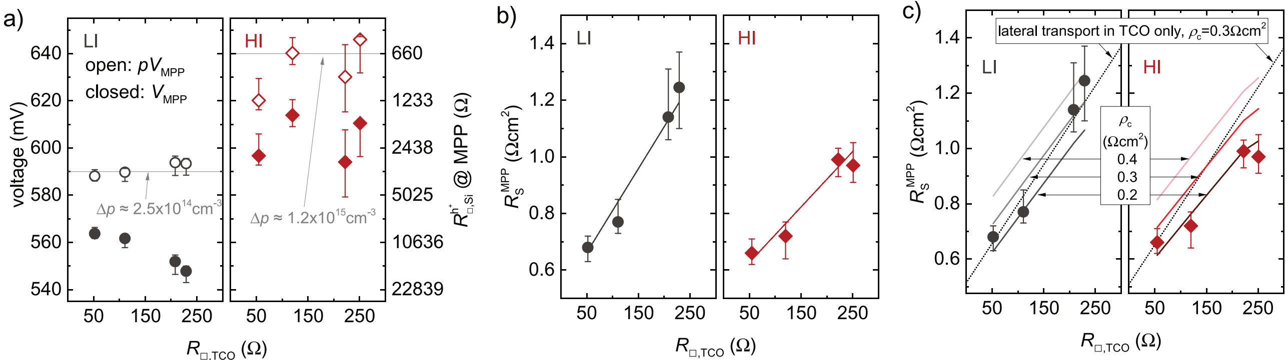

FIG. 7. Data for low-injection (LI) and high-injection (HI) solar cells. (a) V_{MPP} and pV_{MPP}, as well as indicated minority-carrier densities Δp at the respective pV_{MPP}, (b) R_S^{MPP} plus linear fits to the data, (c) calculation of R_S^{MPP}, taking into account only $R_{\square,TCO}$ for lateral transport (dashed line), as well as R_S^{MPP} calculated from the model for three different ρ_c values (solid lines).

carrier absorption in the front ITO, and both LI and HI devices feature the same J_{SC} as expected.

The fill-factor is reduced with increasing $R_{\square,TCO}$ for the LI devices. This trend cannot be seen for the HI devices, as their curves scatter more than the ones of the LI devices. From the presentation of pV_{MPP} in Fig. 7(a), it can be seen that the scattering of *FF* is due to the scattering of pV_{MPP}, probably as a result of varying passivation at MPP within the HI group. That scattering of the passivation is higher for the HI devices and can also be seen from the V_{OC}, which scatters less for the LI vs the HI devices. This hardly avoidable scattering in a non-production environment can be attributed to processing inaccuracies, mostly impacting the HI devices since they are more sensitive to variation in passivation quality.

The slope of R_S^{MPP} vs $R_{\square,TCO}$ was obtained from linear fitting and is less steep for the HI vs the LI devices [cf. Fig. 7(b)]. This indicates that lateral conductivity is higher for the HI devices. With R_S^{MPP} we calculated the pseudo-voltage at maximum power point (pV_{MPP}) using Eq. (B3). As can be seen from Fig. 7(a), pV_{MPP} is about 50 mV higher for the HI devices, resulting in a one order of magnitude higher minority charge carrier density Δp, calculated for 590 mV (LI) and 640 mV (HI), with Eq. (B4), assuming perfect selectivity.[38] We use Δp and Eq. (B2) to calculate $R^{h^+}_{\square,Si}$ and added it as a right y axis of Fig. 7(a). $R^{h^+}_{\square,Si}$ is three to four times lower for the HI vs the LI devices. Using this $R^{h^+}_{\square,Si}$ and the measured $R_{\square,TCO}$, we calculated R_S^{lat+c} for three ρ_c (0.2, 0.3, 0.4 Ω cm^2) for both LI and HI devices. Together with the measured finger (R_S^f) and n-contact (ρ_c^n) resistances, and the calculated vertical resistance for electrons [R_S^{vert}, cf. Eq. (B6)], we sum up the following:

$$R_S^{MPP,\,calc} = R_S^{lat+C} + \underbrace{R_S^f + R_S^{vert} + \rho_c^n}_{R_S^{res}}, \tag{2}$$

with R_S^{res} summing up all residual R_S components. $R_S^{MPP,calc}$ is also included in Fig. 7(c), for the three ρ_c as mentioned above, and for LI and HI devices, respectively. Also included in Fig. 7(c) (dashed line) is a series resistance assuming only lateral transport in the TCO [cf. Eq. (B5)] plus R_S^{res} and 0.3 Ω cm^2 to account for ρ_c^p. The latter R_S calculation fits well the R_S^{MPP} of the LI devices, whereas it overestimates R_S^{MPP} for the HI devices for $R_{\square,TCO}$ in the range of 250 Ω. For the LI devices, the slopes of $R_S^{MPP,calc}$ are a little less steep than for the dashed line, indicating that despite the high $R^{MPP}_{\square,Si}$ some lateral transport is still happening also in the silicon absorber. It is surprising, however, that the dashed line (transport only in TCO) seems to describe the experimental data better than the solid lines (derived from our model). Another interesting point is that a ρ_c of 0.2 Ω cm^2 seems to fit the data of the HI devices better, whereas for the LI devices, the calculations with ρ_c of 0.3 Ω cm^2 seems to describe the experimental data better. This could be simply due to insufficient statistics, or it could indicate that ρ_c of the p-contact is also injection dependent. The lower ρ_c at higher injection could possibly be explained by a higher hole concentration in the *a*-Si(i) layer and thus higher conductivity in this layer. An injection-dependence of ρ_c at the p-contact is also observed in Sec. III B for the solar cell with *a*-Si(p) contact and might be also related to transport in the *a*-Si(i) layer. This is an interesting point that should be investigated in more detail in future work.

B. Deriving the coupling contact resistance

We now consider a different set of experimental devices. The derivation of the p-contact resistance (ρ_c^p) for n-type SHJ solar cells can be done by determining R_S^{MPP}, subsequently subtracting all know R_S-components and assigning the residual resistance to the contact resistance of the p-contact.[17,18,35] In our earlier publication,[18] we compared front-junction SHJ solar cells with *a*-Si(p) and *nc*-Si(p) as a hole-selective layer. It is known from the literature that *nc*-Si(p) should enable a much lower ρ_c than *a*-Si(p).[28,29] In Ref. 18, we showed that neglecting lateral transport in the silicon absorber of these devices would lead to faulty breakdown of

Published under license by AIP Publishing.

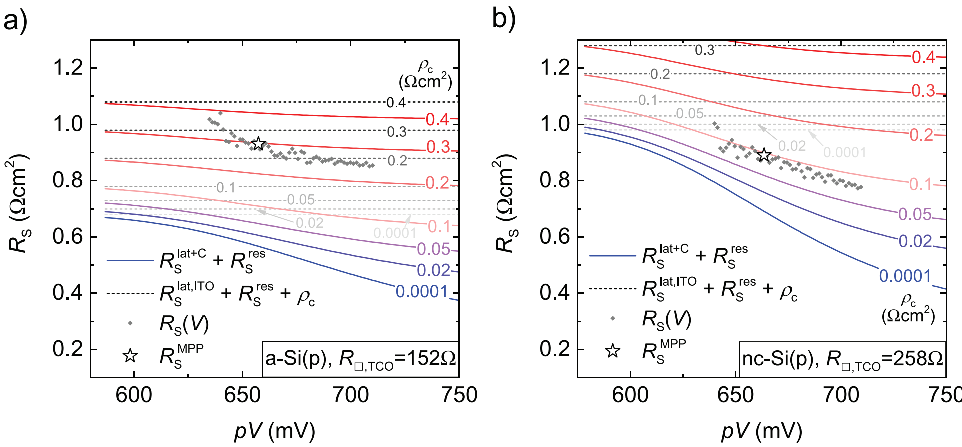

FIG. 8. Series resistance as a function of the pseudo-voltage. (a) For the case of the cell with *a*-Si(p) hole-selective layer, (b) for *nc*-Si(p). Cell data are plotted as gray diamonds, derived from Eq. (B8). Solid lines (red to blue) are calculated from our model, dashed lines (gray shades) assume lateral transport only in the TCO, both for different ρ_c (indicated by the numbers on the lines). R_S^{res} is calculated as shown in Eq. (2).

the R_S losses. However, we assumed $\rho_c = 0\,\Omega\,\text{cm}^2$ for the coupling between silicon absorber and TCO. The work presented here demonstrates that this also leads to faulty results.

In Fig. 8, we show R_S^{lat+c} calculated from our model with the parameters of the two solar cells (cf. caption of Fig. 8). From Suns-V_{OC} and JV measurements, we calculate the pseudo-voltage-dependent series resistance $R_S(pV)$ using Eq. (B8). We can see that $R_S(pV)$ of the *nc*-Si(p)-cell is just slightly below the line of $\rho_c = 0.1\,\Omega\,\text{cm}^2$ at MPP and decreases generally with increasing injection. While $R_S(pV)$ of the *nc*-Si(p)-cell follows well the calculated dependence, $R_S(pV)$ of the *a*-Si(p) cell does less, especially for pV below pV_{MPP}. This might be explained by an injection-dependence of ρ_c itself, similar to the previous case, which is not considered in our model.

In Table I, we summarize the contact resistances ρ_c^p of the two solar cells, derived with three different methods. "TCO only" assumes lateral transport only in the TCO [Eq. (B5)]. This method is slightly underestimating ρ_c^p of the *a*-Si(p)-cell and giving a negative value for the *nc*-Si(p) cell. "$R_{\square,\parallel}$" assumes lateral transport in TCO and silicon absorber, neglecting the coupling via ρ_c [Eq. (1)]. In this case, ρ_c^p is overestimated, as the resistance due to lateral transport is underestimated. The model developed for this paper gives a three times lower contact resistance for the *nc*-Si(p)-cell vs the *a*-Si(p)-cell.

TABLE I. The contact resistances ρ_c^p of two SHJ solar cells, derived with three different methods. The solar cells have different hole-selective layers, as indicated in the first column. "TCO only" assumes lateral transport only in the TCO. $\rho_c = 0$ assumes lateral transport in TCO and silicon absorber, with perfect coupling ($\rho_c = 0\,\Omega\,\text{cm}^2$), as in Ref. 18. The last column shows the values for ρ_c^p derived with the model presented in this paper (ρ_c-dependent coupling).

	Derived ρ_c^p		
	TCO only (Ω cm^2)	$R_{\square,\parallel}$ (Ω cm^2)	**This work** (Ω cm^2)
a-Si (p)	0.23	0.36	**0.30**
nc-Si (p)	−0.09	0.24	**0.09**

IV. CONCLUSIONS

We study lateral transport in silicon solar cells. Usually, silicon solar cells comprise highly conductive regions for lateral charge carrier transport toward grid-fingers. We highlight that for well-passivated ($V_{OC} \gg 700$ mV) devices under operation, the concentrations of both charge carrier types in the silicon absorber are high enough to support lateral transport, while for classical devices, such as passivated emitter and rear cells (PERCs), this is usually only the case for the absorber's majority carriers. Using an analytical model, numerical simulation, and experiments, we find that a low contact resistance between the highly conductive region and the silicon absorber is mandatory to enable significant support of the silicon absorber. For majority carriers, e.g., for lateral transport in rear-junction silicon heterojunction (SHJ) solar cells, this had not been previously considered.

We furthermore show that the *pn*-junction does not prevent coupling. For SHJ solar cells, usually the electron-contact can benefit more from lateral conductivity in the silicon absorber due to the often lower contact resistance and the higher mobility of electrons vs holes. This explains the present-day advantage of rear-junction over front-junction devices. The achievement of low-resistive hole-contacts will shrink this advantage. Also for solar cells with high-temperature passivating contacts this advantage might not be present due to the low contact resistances achieved for both electron- and hole-contacts. For solar cells featuring such contacts, and based on p-type wafers, we expect significant contributions of the silicon absorber to lateral minority-carrier transport due to the higher mobility of electrons and the low contact resistance.

The model developed in this paper should allow for the determination of the *pn*-junction's contact resistance not only via subtracting all known R_S-components from R_S^{MPP}, as done in Sec. III B and Ref. 17, but also from fitting a series with varying pitch of the finger-grid at the contact of interest, using ρ_c as the fitting parameter. In this paper, we applied the model only to mono-facial SHJ solar cells, calculating the effective R_S of the front contact. The model can also be used in the same way for bi-facial cells to calculate one series resistance component for each contact.

Published under license by AIP Publishing.

ACKNOWLEDGMENTS

The authors thank Christophe Allebe, Patrick Wyss, and Nicolas Badel from CSEM for high-quality wet-processing and metallization and Vincent Paratte, Aymeric Schafflützel, and Cédric Bucher for setting the necessary conditions for high-quality cell processing. Many thanks to Laurie-Lou Senaud for proofreading the mathematics of our model. J.H. wishes to thank Olivier Dupré for the idea of plotting voltage-dependent R_S (you knew it must be useful for something, *et voilà*!) and Bernd Rech for his encouragement to share knowledge fast vs exhaustive in-depth simmering. This project has received funding from the European Union's Horizon 2020 research and innovation program under Grant Agreement No. 745601 (Ampere) as well as Swiss National Science Foundation under Ambizione Energy grant PZENP2_173627 ICONS.

APPENDIX A: DESCRIPTION OF THE EQUATION SYSTEM TO SOLVE TWO SHEET RESISTANCES COUPLED VIA A CONTACT RESISTANCE

Figure 1(b) shows the description of the current extraction in a typical solar cell front contact over one base element of the metal grid pattern of pitch L. Homogeneously generated current in the wafer of total value I_0 ($\delta I = \frac{I_0}{L}\,dz$) is extracted to a finger of width l. The current travels both in the wafer and the TCO, whose sheet resistance are $R_{\square,\mathrm{Si}}$ and $R_{\square,\mathrm{TCO}}$, respectively. These two elements are connected together by a contact resistivity ρ_c, accounting for the contact properties of the a-Si:H contact in the case of this paper. Contact between TCO and finger is characterized by a contact resistivity $\rho_c^{\mathrm{TCO/Ag}}$. We chose here to solve the system for homogeneous generation in the wafer, but it can also be solved similarly considering no generation under the finger. The best choice between these to cases is debatable because in real cells there is generation under the fingers because of texturing and exact generation profile is complex. In any case, owing to the small area fraction of the metal grid and the fact that resistive losses for current generated under the contact will contribute less to the series resistance than current generated away from it, the differences between the two approaches is expected to be low.

To get the series resistance $R_S^{\mathrm{lat+c}}$ at device scale, it is needed to calculate the total Joule power loss P_{tot} in the system. For that we need to know the current and the voltage at every position in the wafer and the TCO [$I_2(z)$, $V_2(z)$ and $I_1(z)$, $V_1(z)$, respectively]. Then, we have

$$P_W = \frac{R_{\square,\mathrm{Si}}}{w}\int_0^L {I_2}^2(z)dz, \tag{A1}$$

$$P_{TCO} = \frac{R_{\square,\mathrm{TCO}}}{w}\int_0^L {I_1}^2(z)dz, \tag{A2}$$

$$P_{W/TCO} = \frac{w}{\rho_c}\int_0^L (V_1(z) - V_2(z))^2\,dz, \tag{A3}$$

$$P_C = \frac{w}{\rho_c^{\mathrm{TCO/Ag}}}\int_{\frac{L-l}{2}}^{\frac{L+l}{2}} {V_1}^2(z)dz, \tag{A4}$$

$$P_{tot} = P_W + P_{TCO} + P_{W/TCO} + P_C, \tag{A5}$$

$$R_S^{\mathrm{lat+c}} = \frac{P_{tot}}{{I_0}^2}Lw, \tag{A6}$$

with w is the lateral dimension of the system. The configuration of the present system is very similar to the double layer TLM case and the process to solve it is also very similar, in fact the homogeneous part of the differential equations appearing here are the same than in Ref. 19.

Before starting the resolution, it is worth noting that because of the periodicity of the contact structure, we have planes of symmetry in $z = 0, \frac{L}{2}$, hence in those positions, we have $I_1 = I_2 = 0$. We can, therefore, solve the system between 0 and $\frac{L}{2}$, assuming no contribution from the rest of the system.

1. Outside grid

Using Kirchhoff's current law and Ohm's law we get

$$dI_1 = (V_2(z) - V_1(z))\frac{w}{\rho_c}\,dz, \tag{A7}$$

$$dI_2 = (V_1(z) - V_2(z))\frac{w}{\rho_c}\,dz + \delta I, \tag{A8}$$

$$dV_1 = -R_{\square,\mathrm{TCO}} I_1(z)\frac{dz}{w}, \tag{A9}$$

$$dV_2 = -R_{\square,\mathrm{Si}} I_2(z)\frac{dz}{w}. \tag{A10}$$

All the current generated from the left will be collected in the central printed area, this means that we have $I_1 + I_2 = I_0\frac{z}{L}$. Dividing Eq. (A7) by dz, differentiating it, substituting voltage terms using Eqs. (A9) and (A10), and using this condition, we can deduce that the differential equation followed by I_1 is

$$\frac{d^2 I_1}{dz^2} = \frac{R_{\square,\mathrm{TCO}} + R_{\square,\mathrm{Si}}}{\rho_c} I_1(z) - \frac{R_{\square,\mathrm{Si}} I_0}{\rho_c}\frac{z}{L}. \tag{A11}$$

This is easily solved and we obtain

$$I_1(z) = -\left(d_1 e^{\xi_c z} + d_2\,e^{-\xi_c z}\right) + \frac{R_{\square,\mathrm{Si}} I_0}{R_{\square,\mathrm{TCO}} + R_{\square,\mathrm{Si}}}\frac{z}{L}, \tag{A12}$$

$$I_2(z) = d_1\,e^{\xi_c z} + d_2\,e^{-\xi_c z} + \frac{R_{\square,\mathrm{TCO}} I_0}{R_{\square,\mathrm{TCO}} + R_{\square,\mathrm{Si}}}\frac{z}{L}, \tag{A13}$$

$$V_1(z) = -\frac{R_{\square,\mathrm{TCO}}}{\xi_c w}\left(-d_1\,e^{\xi_c z} + d_2\,e^{-\xi_c z}\right) - (R_{\square,\mathrm{TCO}} \parallel R_{\square,\mathrm{Si}})\frac{I_0 z^2}{2wL} + d3, \tag{A14}$$

$$V_2(z) = -\frac{R_{\square,\mathrm{Si}}}{\xi_c w}\left(d_1\,e^{\xi_c z} - d_2\,e^{-\xi_c z}\right) - (R_{\square,\mathrm{TCO}} \parallel R_{\square,\mathrm{Si}})\frac{I_0 z^2}{2wL} + d4, \tag{A15}$$

with $\xi_c = \sqrt{\frac{R_{\square,\mathrm{TCO}}+R_{\square,\mathrm{Si}}}{\rho_c}}$, $(R_{\square,\mathrm{TCO}} \parallel R_{\square,\mathrm{Si}}) = \frac{R_{\square,\mathrm{TCO}}R_{\square,\mathrm{Si}}}{R_{\square,\mathrm{TCO}}+R_{\square,\mathrm{Si}}}$, and d_1, d_2, d_3, d_4 constants to be determined from continuity and boundary condition.

Published under license by AIP Publishing.

2. Under grid

Similar to outside the grid contact, we get

$$dI_{C1} = (V_{C2}(z) - V_{C1}(z))\frac{w}{\rho_c}\,dz - V_{C1}(z)\frac{w}{\rho_c^{TCO/Ag}}\,dz, \quad (A16)$$

$$dI_{C2} = (V_{C1}(z) - V_{C2}(z))\frac{w}{\rho_c}\,dz + \delta I, \quad (A17)$$

$$dV_{C1} = -R_{\square,TCO} I_{C1}(z)\frac{dz}{w}, \quad (A18)$$

$$dV_{C2} = -R_{\square,Si} I_{C2}(z)\frac{dz}{w}. \quad (A19)$$

We use the same process than previously to separate current and voltage terms combining (A16), (A17), (A18), and (A19). This time, however, we get a coupled system to solve for I_{c1} and I_{c2},

$$\begin{bmatrix} \frac{d^2 I_{C1}}{dz^2} \\ \frac{d^2 I_{C2}}{dz^2} \end{bmatrix} = \begin{bmatrix} \frac{R_{\square,TCO}}{\rho_c} + \frac{R_{\square,TCO}}{\rho_c^{TCO/Ag}} & -\frac{R_\square}{\rho_c} \\ -\frac{R_{\square,TCO}}{\rho_c} & \frac{R_\square}{\rho_c} \end{bmatrix} \begin{bmatrix} I_{C1}(z) \\ I_{C2}(z) \end{bmatrix}. \quad (A20)$$

To solve this system, we use a bit of linear algebra. The eigenvalues of the matrix in Eq. (A20) are

$$H_{p,n} = \frac{1}{2}\left(\frac{R_{\square,TCO}}{\rho_c^{TCO/Ag}} + \xi_c^{\,2} \pm \sqrt{\left(\frac{R_{\square,TCO}}{\rho_c^{TCO/Ag}} + \xi_c^2\right)^2 - 4\frac{(R_{\square,TCO} \parallel R_{\square,Si})}{\rho_c^{TCO/Ag}}\xi_c^{\,2}} \right) \quad (A21)$$

and the associated eigenvectors are $u_{p,n} = \begin{bmatrix} 1 \\ \lambda_{p,n} \end{bmatrix}$ with

$$\lambda_{p,n} = \frac{R_{\square,TCO}}{R_{\square,Si} - \rho_c H_{p,n}}. \quad (A22)$$

Then, the solution to the system is

$$\begin{bmatrix} I_{C1}(z) \\ I_{C2}(z) \end{bmatrix} = \left(a_p e^{\eta_p z} + b_p e^{-\eta_p z}\right)\begin{bmatrix} 1 \\ \lambda_p \end{bmatrix} + \left(a_n e^{\eta_n z} + b_n e^{-\eta_n z}\right)\begin{bmatrix} 1 \\ \lambda_n \end{bmatrix}, \quad (A23)$$

with $\eta_{p,n} = \sqrt{H_{p,n}}$ $V_{C1}(z)$ and $V_{C2}(z)$ can be obtained integrating Eqs. (A18) and (A19), and the integration constants can be deduced from Eqs. (A16) and (A17) that we can combine to obtain $V_{C1}(z)$ and $V_{C2}(z)$ separately,

$$V_{C1}(z) = -\frac{\rho_c^{TCO/Ag}}{w}\left(\frac{dI_{C1}}{dz} + \frac{dI_{C2}}{dz}\right) + \frac{\rho_c^{TCO/Ag}}{w}\frac{\delta I}{dz}, \quad (A24)$$

$$V_{C2}(z) = -\frac{\rho_c^{TCO/Ag}}{w}\frac{dI_{C1}}{dz} - \frac{\rho_c + \rho_c^{TCO/Ag}}{w}\frac{dI_{C2}}{dz} + \frac{\rho_c + \rho_c^{TCO/Ag}}{w}\frac{\delta I}{dz}. \quad (A25)$$

The last term in each equation is obviously our integration constant, so we can finally integrate Eqs. (A18) and (A19)

$$V_{C1}(z) = -\frac{R_{\square,TCO}}{w\eta_p}\left(a_p\, e^{\eta_p z} - b_p\, e^{-\eta_p z}\right) - \frac{R_{\square,TCO}}{w\eta_n}\left(a_n\, e^{\eta_n z} - b_n\, e^{-\eta_n z}\right) + \frac{\rho_c^{TCO/Ag}}{w}\frac{I_0}{L}, \quad (A26)$$

$$V_{C2}(z) = -\frac{R_{\square,Si}\lambda_p}{w\eta_p}\left(a_p\, e^{\eta_p z} - b_p\, e^{-\eta_p z}\right) - \frac{R_{\square,Si}\lambda_n}{w\eta_n}\left(a_n\, e^{\eta_n z} - b_n\, e^{-\eta_n z}\right) + \frac{\rho_c + \rho_c^{TCO/Ag}}{w}\frac{I_0}{L}. \quad (A27)$$

3. Continuity and boundary conditions

We now need to determine d_1, d_2, d_3, d_4, a_p, b_p, a_n, and b_n. For that we know already that $I_1(0) = I_2(0) = 0$, which gives a first condition, as the condition is redundant. We also know $I_{C1}\left(\frac{L}{2}\right) = I_{C1}\left(\frac{L}{2}\right) = 0$, which gives two more conditions. We also have the continuity of the current and voltage in the wafer and TCO at $z = \frac{L-l}{2}$ that gives four more conditions. The last condition is obtained by noticing that Eqs. (A8) and (A17) have the same form and depend only on the voltages and δI, which are all continuous. The last condition is, therefore, that $\frac{dI_2}{dz}$ is continuous with $\frac{dI_{C2}}{dz}$ at $z = \frac{L-l}{2}$. All the parameters can, therefore, be obtained by solving the linear system created by all these boundary conditions, and then $I_1(z)$, $V_1(z)$, $I_2(z)$, and $V_2(z)$ can be evaluated at any position and the R_S^{lat+c} calculated using Eqs. (A1), (A2), (A3), (A4), (A5), and (A6).

4. Simplification of the linear system

The linear system from boundary and continuity conditions can be simplified by using the boundary conditions: using $I_1(0) = I_2(0) = 0$, we have $d_1 = -d_2$. Also changing the origin by using $z' = z - \frac{L}{2}$ for the currents and voltages below the grid and using $I_1\left(z = \frac{L}{2}\right) = I_2\left(z = \frac{L}{2}\right) = 0$, we have $a_p = -b_p$ and $a_n = -b_n$. Equations are

$$I_1(z) = -\alpha_1 \sinh(\xi_c z) + \frac{R_{\square,Si} I_0}{R_{\square,TCO} + R_{\square,Si}}\frac{z}{L}, \quad (A28)$$

$$I_2(z) = \alpha_1 \sinh(\xi_c z) + \frac{R_{\square,TCO} I_0}{R_{\square,TCO} + R_{\square,Si}}\frac{z}{L}, \quad (A29)$$

$$V_1(z) = \frac{R_{\square,TCO}}{\xi_c w}\alpha_1 \cosh(\xi_c z) - (R_{\square,TCO} \parallel R_{\square,Si})\frac{I_0 z^2}{2wL} + d3, \quad (A30)$$

$$V_2(z) = -\frac{R_{\square,Si}}{\xi_c w}\alpha_1 \cosh(\xi_c z) - (R_{\square,TCO} \parallel R_{\square,Si})\frac{I_0 z^2}{2wL} + d4, \quad (A31)$$

$$I_{C1}(z') = \alpha_p \sinh\left(\eta_p z'\right) + \alpha_n \sinh(\eta_n z'), \quad (A32)$$

Published under license by AIP Publishing.

$$I_{C2}(z') = \lambda_p \alpha_p \sinh\left(\eta_p z'\right) + \lambda_n \alpha_n \sinh(\eta_n z'), \tag{A33}$$

$$V_{C1}(z') = -\frac{R_{\square,\mathrm{TCO}}}{w\eta_p} \alpha_p \cosh\left(\eta_p z'\right) - \frac{R_{\square,\mathrm{TCO}}}{w\eta_n} \alpha_n \cosh(\eta_n z') + \frac{\rho_c^{\mathrm{TCO/Ag}}}{w} \frac{I_0}{L}, \tag{A34}$$

$$V_{C2}(z') = -\frac{R_{\square,\mathrm{Si}}\lambda_p}{w\eta_p} \alpha_p \cosh\left(\eta_p z'\right) - \frac{R_{\square,\mathrm{Si}}\lambda_n}{w\eta_n} \alpha_n \cosh(\eta_n z') + \frac{\rho_c + \rho_c^{\mathrm{TCO/Ag}}}{w} \frac{I_0}{L}. \tag{A35}$$

The linear system of the boundary condition is then

$$\begin{bmatrix} -\sinh\left(\xi_c \frac{L-l}{2}\right) & 00 & -\sinh\left(\eta_p \frac{-l}{2}\right) & -\sinh\left(\eta_n \frac{-l}{2}\right) \\ \sinh\left(\xi_c \frac{L-l}{2}\right) & 00 & -\lambda_p \sinh\left(\eta_p \frac{-l}{2}\right) & -\lambda_n \sinh\left(\eta_n \frac{-l}{2}\right) \\ \frac{R_{\square,\mathrm{TCO}}}{\xi_c w} \cosh\left(\xi_c \frac{L-l}{2}\right) & 10 & \frac{R_{\square,\mathrm{TCO}}}{w\eta_p} \cosh\left(\eta_p \frac{-l}{2}\right) & \frac{R_{\square,\mathrm{TCO}}}{w\eta_n} \cosh\left(\eta_n \frac{-l}{2}\right) \\ \frac{-R_{\square,\mathrm{Si}}}{\xi_c w} \cosh\left(\xi_c \frac{L-l}{2}\right) & 01 & \frac{R_{\square,\mathrm{Si}}\lambda_p}{w\eta_p} \cosh\left(\eta_p \frac{-l}{2}\right) & \frac{R_{\square,\mathrm{Si}}\lambda_n}{w\eta_n} \cosh\left(\eta_n \frac{-l}{2}\right) \\ \xi_c \cosh\left(\xi_c \frac{L-l}{2}\right) & 00 & -\lambda_p \eta_p \cosh\left(\eta_p \frac{-l}{2}\right) & -\lambda_n \eta_n \cosh\left(\eta_n \frac{-l}{2}\right) \end{bmatrix} \begin{bmatrix} \alpha_1 \\ d_3 \\ d_4 \\ \alpha_p \\ \alpha_n \end{bmatrix} = \begin{bmatrix} -\frac{R_{\square,\mathrm{Si}} I_0}{R_{\square,\mathrm{TCO}} + R_{\square,\mathrm{Si}}} \frac{L-l}{2L} \\ -\frac{R_{\square,\mathrm{TCO}} I_0}{R_{\square,\mathrm{TCO}} + R_{\square,\mathrm{Si}}} \frac{L-l}{2L} \\ (R_{\square,\mathrm{TCO}} \parallel R_{\square,\mathrm{Si}}) \frac{I_0 (L-l)^2}{8wL} + \frac{\rho_c^{\mathrm{TCO/Ag}}}{w} \frac{I_0}{L} \\ (R_{\square,\mathrm{TCO}} \parallel R_{\square,\mathrm{Si}}) \frac{I_0 (L-l)^2}{8wL} + \frac{\rho_c + \rho_c^{\mathrm{TCO/Ag}}}{w} \frac{I_0}{L} \\ -\frac{R_{\square,\mathrm{TCO}}}{R_{\square,\mathrm{TCO}} + R_{\square,\mathrm{Si}}} \frac{I_0}{L} \end{bmatrix}. \tag{A36}$$

This system can be solved, and, in principle, it is possible to obtain analytic expressions for all the desired coefficients, then do the integrations of Eqs. (A1), (A2), (A3), and (A4), to finally get an analytical expression for $R_S^{\mathrm{lat+c}}$. This is, however, not very practical because the final formula will be very complex. It is more sensible to substitute the expressions in Eq. (A36) by their numerical values, solve it, and then numerically calculate the power loss and $R_S^{\mathrm{lat+c}}$. Due to the simplifications done, power losses became

$$P_W = 2\frac{R_{\square,\mathrm{Si}}}{w} \left(\int_0^{\frac{L-l}{2}} {I_2}^2(z) dz + \int_{\frac{-l}{2}}^0 {I_{C2}}^2(z') dz' \right), \tag{A37}$$

$$P_{TCO} = 2\frac{R_{\square,\mathrm{TCO}}}{w} \left(\int_0^{\frac{L-l}{2}} {I_1}^2(z) dz + \int_{\frac{-l}{2}}^0 {I_{C1}}^2(z') dz' \right), \tag{A38}$$

$$P_{W/TCO} = \frac{2w}{\rho_c} \left(\int_0^{\frac{L-l}{2}} (V_1(z) - V_2(z))^2 dz + \int_{\frac{-l}{2}}^0 (V_{C1}(z') - V_{C2}(z'))^2 dz' \right), \tag{A39}$$

$$P_C = \frac{2w}{\rho_c^{\mathrm{TCO/Ag}}} \int_{\frac{-l}{2}}^0 {V_{C1}}^2(z') dz'. \tag{A40}$$

APPENDIX B: ADDITIONAL FORMULAS USED FOR THE CALCULATIONS

The relevant input parameters of the model are the sheet resistance of the TCO, $R_{\square,\mathrm{TCO}}$, the sheet resistance of the silicon absorber, $R_{\square,\mathrm{Si}}$, for the relevant carrier species, thus $R_{\square,\mathrm{Si}}^{h^+}$ or $R_{\square,\mathrm{Si}}^{e^-}$and the contact resistance between silicon and TCO ρ_c. While $R_{\square,\mathrm{TCO}}$ can be measured, e.g., with the four-point-probe technique, for a silicon solar cell, $R_{\square,\mathrm{Si}}$ is more difficult to access. Generally, the conductivity $\sigma_{e/h}$ for electrons (e) or holes (h) in a material can be calculated with

$$\sigma_{e/h} = q \cdot n_{e/h} \cdot \mu_{e/h}, \tag{B1}$$

where q is the elementary charge, $n_{e/h}$ is the concentration of electrons or holes, and $\mu_{e/h}$ is the mobility.

Then, the sheet resistance for electrons (e) or holes (h) in a silicon absorber of thickness t_{Si} can be calculated with

$$R_{\square,\,\mathrm{Si}}^{e^-/h^+} = \frac{1}{\sigma_{e/h} \cdot t_{\mathrm{Si}}}. \tag{B2}$$

The total concentration of, e.g., electrons is $n_e = n_0 + \Delta n$ with the electron concentration in equilibrium n_0, and the excess charge carrier density Δn (and for holes accordingly). The excess charge carrier density is injection dependent and can be calculated from the difference of the quasi-Fermi levels, i.e., the so-called implied voltage of the silicon absorber[34] [Eq. (2)]. For high enough selectivity, the implied voltage equals the pseudo-voltage pV, which can be measured with a Suns-V_{OC} measurement.[39] If the series resistance at a certain voltage is known, pV can also be calculated using Eq. (B3),

$$pV = V + J(V) \cdot R_S(V). \tag{B3}$$

When not limited by selectivity,[38] the pseudo-voltage equals the implied voltage V_{impl} and is thus corresponding to the splitting of the quasi-Fermi-levels. With this, the excess charge carrier density Δn can be calculated following Eq. (B4),[40]

$$\Delta n = \sqrt{\frac{(n_0 + p_0)^2}{4} + n_0\, p_0\, e^{\frac{q \cdot V_{\mathrm{impl}}}{k_B T}} - n_0\, p_0} - \frac{n_0 + p_0}{2}, \tag{B4}$$

Published under license by AIP Publishing.

with $n_0 = N_D$ and $p_0 = n_i^2/N_D$ for an n-type silicon absorber, k_B the Boltzmann constant, and the absolute temperature T.

The series resistance due to lateral transport in a conductive layer, with a current injected homogeneously from below, and flowing toward one end of the unit cell can be calculated with Ref. 41, Eq. (41). In the case of SHJ solar cells, this would refer to lateral transport only in one layer (i.e., the TCO), where p is the grid-finger distance and $R_{\square,\mathrm{TCO}}$ is the sheet resistance of the TCO,

$$R_{\mathrm{S,lat}}^{\mathrm{TCO}} = \frac{1}{12} p^2 R_{\square,\mathrm{TCO}}. \quad \text{(B5)}$$

The vertical resistance R_S^{vert} can be estimated with the specific resistivity for electrons or holes $\rho_{\mathrm{Si}}^{e/h}$ and the thickness of the silicon absorber with

$$R_S^{\mathrm{vert,\,e/h}} = \rho_{\mathrm{Si}}^{e/h}\, t_{\mathrm{Si}}. \quad \text{(B6)}$$

From the resistance between the two external busbars and Eq. (B7), the finger resistance can be calculated with the line resistance of a finger R_{line}^{f} in $\Omega\,\mathrm{cm}^{-1}$, the pitch p, and the finger length, l_f,

$$R_S^{f} = \frac{1}{3} p\, l_f^2\, R_{\mathrm{line}}^{f}. \quad \text{(B7)}$$

The pseudo-voltage-dependent R_S was calculated from the R_S-free pseudo-JV-curve obtained from a Suns-V_{OC} measurement,[39] and the JV-curve from measurement at STC, as described in Eq. (B8),

$$R_S(pV) = \frac{pV(J) - V(J)}{J}. \quad \text{(B8)}$$

APPENDIX C: DESCRIPTION OF THE SIMULATION APPROACH

The numerical simulations presented in this paper are carried out using Sentaurus TCAD, which allows the implementation of various models necessary for modeling silicon heterojunction devices.[42] Analogous to the experimental solar cells, we used an n-type silicon absorber with a resistivity of $2\,\Omega\,\mathrm{cm}$ and a thickness of $180\,\mu$m. The front-junction is a standard SHJ layer stack of intrinsic amorphous silicon *a*-Si(i), p-type amorphous silicon *a*-Si (p), and a transparent conductive oxide TCO(n^{++}), which accounts for lateral transport toward the metal contacts. The TCO is modeled as a 100 nm thick conductive layer with a low-ohmic contact toward the *a*-Si(p) layers. The front finger has a width of $50\,\mu$m, and the front finger-pitch is $1850\,\mu$m. The defects in all *a*-Si layers are assumed as in Ref. 43. The rear contact is a low-ohmic standard SHJ layer with 5 nm *a*-Si(i), 10 nm *a*-Si(n), and full-area metal contact. At the interface of the *c*-Si(n) bulk and *a*-Si(i) passivation layer, we assume an effective surface recombination velocity with S_0 varied from $0\,\mathrm{cm\,s^{-1}}$ to $10^7\,\mathrm{cm\,s^{-1}}$ in order to investigate the differences in lateral transport for different injection conditions within the silicon absorber. For the local metal finger at front side, we assumed a contact resistivity of $6.8\,\mathrm{m}\Omega\,\mathrm{cm}^2$; for the full-area rear contact, we assumed a contact resistivity of $250\,\mathrm{m}\Omega\,\mathrm{cm}^2$. Simulation models and parameters, which were used for the Sentaurus TCAD model are listed in Table II and are based on Ref. 42.

TABLE II. Physical models and parameter set for the Sentaurus TCAD simulation model.

Sentaurus TCAD version	L-2016.03-SP2
Physical models	
Thermionic emission	References 42, p. 771 and 44
Silicon: bandgap	Paessler[45]
Silicon: density of states masses	Green[46] and Couderc[47]
Silicon: auger	Richter[48]
Global	
Temperature	298.15 K
Spectrum	AM1.5g
TCO, *described as conductor*	
Thickness	100 nm
Sheet resistance	varied
Doped amorphous silicon a-Si(p/n)	
Thickness	10 nm
Activation energy	200 meV for p-type, 150 meV for n-type
Trap concentrations	As in Ref. 43
Intrinsic amorphous silicon a-Si(i)	
Thickness	5 nm
Trap concentrations	As in Ref. 43
Crystalline silicon bulk	
Thickness	180 μm
Resistivity	2 Ω cm, n-type

APPENDIX D: DETAILS ON MODEL VALIDATION

To derive R_S^{MPP} for the JV-curves simulated with Sentaurus TCAD, we used the common method from the literature with two illumination levels[36,37] as for the experimental devices. To be able to apply the method, we simulated two JV-curves, one at 1 sun and the other at 0.05 sun. With R_S^{MPP}, as well as voltage (V_{MPP}) and current density (J_{MPP}) at MPP, we calculate the pseudo-voltage at MPP pV_{MPP} with Eq. (B3). When selectivity is not limiting, pV_{MPP} equals iV_{MPP}.

TABLE III. Series resistance values and components used for the validation of our model.

Condition	R_S^{vert}@MPP ($\Omega\,\mathrm{cm}^2$)	R_S rear ($\Omega\,\mathrm{cm}^2$)	$R_{\square,\mathrm{Si}}^{h^+}$ (Ω)
604 mV	0.035	0.25	30 597
635 mV	0.035	0.25	9741
669 mV	0.032	0.25	2806
732 mV	0.021	0.25	400
752 mV	0.014	0.25	192

Published under license by AIP Publishing.

From iV_{MPP}, we calculate the excess charge carrier density using Eq. (B4) and use it as input to calculate the hole conductivity with Eq. (B1) and from that $R_{\square,\mathrm{Si}}^{\mathrm{h}^+}$ with Eq. (B2). The calculated $R_{\square,\mathrm{Si}}^{\mathrm{h}^+}$ values are given in Table III for reference. We then use $R_{\square,\mathrm{Si}}^{\mathrm{h}^+}$ as input for our model to calculate $R_{\mathrm{S}}^{\mathrm{lat+c}}$.

As our model does not contain an R_{S}-component due to vertical transport of the electrons but the $R_{\mathrm{S}}^{\mathrm{MPP}}$ obtained for the numerical simulation obviously does, we calculated $R_{\mathrm{S}}^{\mathrm{vert}}$ for each injection condition using Eq. (B6). The derived $R_{\mathrm{S}}^{\mathrm{vert}}$ are summarized in Table III. Additionally, in the simulation a contact resistance of $0.25\,\Omega\,\mathrm{cm}^2$ was assumed for the full-area rear contact. To be comparable with the $R_{\mathrm{S}}^{\mathrm{MPP}}$ values obtained from the simulation, we add this as well to the R_{S} calculated with our model.

REFERENCES

[1] A. Cuevas and D. Yan, IEEE J. Photovoltaics **3**, 916 (2013).
[2] F. Feldmann, M. Simon, M. Bivour, C. Reichel, M. Hermle, and S. W. Glunz, Sol. Energy Mater. Sol. Cells **131**, 100 (2014).
[3] U. Römer, R. Peibst, T. Ohrdes, B. Lim, J. Krügener, E. Bugiel, T. Wietler, and R. Brendel, Sol. Energy Mater. Sol. Cells **131**, 85 (2014).
[4] A. Ingenito, G. Nogay, Q. Jeangros, E. Rucavado, C. Allebé, S. Eswara, N. Valle, T. Wirtz, J. Horzel, T. Koida, M. Morales-Masis, M. Despeisse, F. J. Haug, P. Löper, and C. Ballif, Nat. Energy **3**, 800 (2018).
[5] J. Haschke, O. Dupré, M. Boccard, and C. Ballif, Sol. Energy Mater. Sol. Cells **187**, 140 (2018).
[6] J. Dréon, Q. Jeangros, J. Cattin, J. Haschke, L. Antognini, C. Ballif, and M. Boccard, Nano Energy **70**, 104495 (2020).
[7] A. Cuevas, Prog. Photovoltaics Res. Appl. **22**, 764 (2014).
[8] R. Schwartz, M. Lundstrom, and R. Nasby, IEEE Trans. Electron Devices **28**, 264 (1981).
[9] R. Swanson, S. Beckwith, R. Crane, W. Eades, Y. H. Kwark, R. Sinton, and S. Swirhun, IEEE Trans. Electron Devices **31**, 661 (1984).
[10] F. Granek, M. Hermle, D. M. Huljic, O. Schultz-Wittmann, and S. W. Glunz, Prog. Photovoltaics Res. Appl. **17**, 47 (2009).
[11] M. Bivour, S. Schröer, M. Hermle, and S. W. Glunz, Sol. Energy Mater. Sol. Cells **122**, 120 (2014).
[12] H. Park, Y. J. Lee, J. Park, Y. Kim, J. Yi, Y. Lee, S. Kim, C. K. Park, and K. J. Lim, Trans. Electr. Electron. Mater. **19**, 165 (2018).
[13] L. Basset, W. Favre, D. Muñoz, and J. P. Vilcot, in *Proceedings of the 35th European Photovoltaic Solar Energy Conference* (WIP GmbH & Co Planungs-KG, 2018), pp. 721–724.
[14] L. Yang, S. Zhong, W. Zhang, X. Li, Z. Li, Y. Zhuang, X. Wang, L. Zhao, X. Cao, X. Deng, Q. Wang, and W. Shen, Prog. Photovoltaics Res. Appl. **26**, 385 (2018).
[15] A. Cruz, E. C. Wang, A. B. Morales-Vilches, D. Meza, S. Neubert, B. Szyszka, R. Schlatmann, and B. Stannowski, Sol. Energy Mater. Sol. Cells **195**, 339 (2019).
[16] A. G. Aberle, S. R. Wenham, and M. A. Green, in *Conference Record of the Twenty Third IEEE Photovoltaic Specialists Conference—1993 (Cat. No. 93CH3283-9)* (IEEE, 1993), pp. 133–139.
[17] E.-C. Wang, A. B. Morales-vilches, S. Neubert, R. Schlatmann, and B. Stannowski, AIP Conf. Proc. **2147**, 040022 (2019).
[18] J. Haschke, C. Messmer, J. Cattin, M. Bivour, M. Boccard, and C. Ballif, in *Proceedings of the 46th IEEE Photovoltaic Specialists Conference* (IEEE, Chicago, 2019).
[19] K. C. Huang, D. B. Janes, K. J. Webb, and M. R. Melloch, IEEE Trans. Electron Devices **43**, 676 (1996).
[20] K. Yoshikawa, W. Yoshida, T. Irie, H. Kawasaki, K. Konishi, H. Ishibashi, T. Asatani, D. Adachi, M. Kanematsu, H. Uzu, and K. Yamamoto, Sol. Energy Mater. Sol. Cells **173**, 37 (2017).
[21] E. Kobayashi, N. Nakamura, K. Hashimoto, and Y. Watabe, in *Proceedings of the 28th European Photovoltaic Solar Energy Conference and Exhibition* (WIP GmbH & Co Planungs-KG, 2013), pp. 691–694.
[22] D. Meza, A. Cruz, A. Morales-Vilches, L. Korte, and B. Stannowski, Appl. Sci. **9**, 862 (2019).
[23] A. Richter, J. Benick, F. Feldmann, A. Fell, M. Hermle, and S. W. Glunz, Sol. Energy Mater. Sol. Cells **173**, 96 (2017).
[24] F. Haase, C. Hollemann, S. Schäfer, A. Merkle, M. Rienäcker, J. Krügener, R. Brendel, and R. Peibst, Sol. Energy Mater. Sol. Cells **186**, 184 (2018).
[25] G. Nogay, A. Ingenito, E. Rucavado, Q. Jeangros, J. Stuckelberger, P. Wyss, M. Morales-Masis, F.-J. Haug, P. Loper, and C. Ballif, IEEE J. Photovoltaics **8**, 1478 (2018).
[26] Y. Chen, D. Chen, P. P. Altermatt, G. Xu, Z. Wang, C. Liu, Y. Zou, Y. He, Y. Wang, J. Gong, L. Yuan, W. Liu, Y. Chen, M. Deng, Y. Hu, S. Chen, J. Xiang, H. Shen, S. Zhang, L. Wang, X. Zhang, Y. Yang, Z. Feng, and P. J. Verlinden, in *Proceedings of the 36th European Photovoltaic Solar Energy Conference and Exhibition, 9–13 September, Marseille* (WIP GmbH & Co Planungs-KG, 2019), pp. 294–299.
[27] Z. P. Ling, S. Duttagupta, F. Ma, T. Mueller, A. G. Aberle, and R. Stangl, AIP Adv. **5**, 077124 (2015).
[28] S.-Y. Lee, H. Choi, H. Li, K. Ji, S. Nam, J. Choi, S.-W. Ahn, H.-M. Lee, and B. Park, Sol. Energy Mater. Sol. Cells **120**, 412 (2014).
[29] G. Nogay, J. P. Seif, Y. Riesen, A. Tomasi, Q. Jeangros, N. Wyrsch, F. J. Haug, S. De Wolf, and C. Ballif, IEEE J. Photovoltaics **6**, 1654 (2016).
[30] D. Lachenal, D. Baetzner, W. Frammelsberger, B. Legradic, P. Papet, B. Strahm, and G. Wahli, Energy Procedia **92**, 932 (2016).
[31] M. Leilaeioun, W. Weigand, P. Muralidharan, M. Boccard, D. Vasileska, S. Goodnick, and Z. Holman, in *2017 IEEE 44th Photovoltaic Specialist Conference (PVSC)* (IEEE, 2017), pp. 1790–1793.
[32] W. Weigand, A. M. Leilaeioun, T. Ngo, S. Mercado, and Z. C. Holman, in *2018 IEEE 7th World Conference on Photovoltaic Energy Conversion (WCPEC) (A Joint Conference of 45th IEEE PVSC, 28th PVSEC and 34th EU PVSEC)* (IEEE, 2018), pp. 3905–3907.
[33] D. Lachenal, P. Papet, B. Legradic, R. Kramer, T. Kössler, L. Andreetta, N. Holm, W. Frammelsberger, D. Baetzner, B. Strahm, L. Senaud, J. Schüttauf, A. Descoeudres, G. Christmann, S. Nicolay, M. Despeisse, B. Paviet-Salomon, and C. Ballif, Sol. Energy Mater. Sol. Cells **200**, 110036 (2019).
[34] S. De Wolf, A. Descoeudres, Z. C. Holman, and C. Ballif, Green **2**, 7 (2012).
[35] J. Haschke, R. Lemerle, B. Aissa, A. A. Abdallah, M. M. Kivambe, M. Boccard, and C. Ballif, IEEE J. Photovoltaics **9**, 1202 (2019).
[36] S. Bowden and A. Rohatgi, in *Proceedings of the 17th European Photovoltaic Solar Energy Conference* (WIP GmbH & Co Planungs-KG, 2001).
[37] M. Wolf and H. Rauschenbach, Adv. Energy Convers. **3**, 455 (1963).
[38] A. Onno, C. Chen, P. Koswatta, M. Boccard, and Z. C. Holman, J. Appl. Phys. **126**, 183103 (2019).
[39] R. Sinton and A. Cuevas, in *Proceedings of the 16th European Photovoltaic Solar Energy Conference* (WIP GmbH & Co Planungs-KG, 2000).
[40] D. Adachi, J. L. Hernández, and K. Yamamoto, Appl. Phys. Lett. **107**, 233506 (2015).
[41] N. Convers Wyeth, Solid State Electron. **20**, 629 (1977).
[42] Synopsys, Sentaurus device user guide: Release L-2016.03-SP2 (2016).
[43] R. Stangl, M. Kriegel, and M. Schmidt, in *2006 IEEE 4th World Conference on Photovoltaic Energy Conference, Hawaii* (IEEE, 2006), pp. 1350–1353.
[44] D. Schroeder, *Modelling of Interface Carrier Transport for Device Simulation* (Springer Science Business Media, 2013).
[45] R. Pässler, Phys. Rev. B **66**, 085201 (2002).
[46] M. A. Green, J. Appl. Phys. **67**, 2944 (1990).
[47] R. Couderc, M. Amara, and M. Lemiti, J. Appl. Phys. **115**, 093705 (2014).
[48] A. Richter, S. W. Glunz, F. Werner, J. Schmidt, and A. Cuevas, Phys. Rev. B **86**, 165202 (2012).

Published under license by AIP Publishing.